The Planetary Science Journal, 6:63 (17pp), 2025 March https://doi.org/10.3847/PSJ/adba4b

Transport and Mixing in Planetary Polar Vortices with Annular and Monopolar Potential Vorticity Structures

Jacob Shultis[1], William Seviour[2], Darryn Waugh[1], and Anthony Toigo[3]
[1] Department of Earth and Planetary Sciences, Johns Hopkins University, Baltimore, MD 21210, USA
[2] Global Systems Institute and Department of Mathematics and Statistics, University of Exeter, Exeter, EX4 4QE, UK
[3] Johns Hopkins University Applied Physics Laboratory, Laurel, MD 20723, USA
Received 2024 November 4; revised 2025 February 3; accepted 2025 February 18; published 2025 March 20

Abstract

Polar vortices are a common feature in the solar system, but their structure varies between planets. Although polar vortices are characterized by a coherent region of high potential vorticity (PV) in the polar regions, the meridional variation of PV ranges from strong monopolar to annular distributions. The reduced stability of an annular vortex compared to a monopolar vortex may lead to increased horizontal transport between the midlatitudes and the poles, but this has yet to be thoroughly investigated. Here we perform such an investigation by quantifying the horizontal mixing in polar vortices of varying PV structure, for both a two-dimensional shallow-water model and a three-dimensional general circulation model (GCM). Good agreement is found between the models, with both models indicating that both vortices maintain a horizontal mixing barrier that isolates the polar regions from the extratropics. The primary difference between the two vortex structures is on the interior of the vortex edge, where there is increased mixing inside the annular vortex but a clear reduction of mixing inside the monopolar vortex. In the three-dimensional GCM, a "subvortex" region is identified below the annular polar vortex that allows for more transport of material into the polar regions than the subvortex of the monopolar vortex. This suggests a potential pathway for transport into annular vortices that does not occur for monopolar vortices. Although we start from a Mars-like atmosphere for simplicity and flexibility, our results should describe other terrestrial planets/moons with broad polar vortices with coherent regions of high PV.

Unified Astronomy Thesaurus concepts: Polar jets (1274); Atmospheric dynamics (2300); Atmospheric variability (2119); Mars (1007); Titan (2186); Atmospheric circulation (112)

1. Introduction

Polar vortices of a variety of shapes and sizes have been observed on all terrestrial bodies in our solar system that sustain a significant atmosphere (D. M. Mitchell et al. 2021, D. W. Waugh 2023). These polar vortices are generally characterized by a cold pole and strong circumpolar winds that only exist during the winter season but not the summer. On Earth the polar vortex is a prominent feature in our stratospheric circulation, and is closely tied to the formation of the ozone hole over the Antarctic due to its ability to isolate the polar region from the midlatitudes (M. E. McIntyre 1989; R. A. Plumb et al. 2003; D. W. Waugh et al. 2010; D. M. Mitchell et al. 2015; D. W. Waugh 2023). In Mars' middle atmosphere (which does not have a stratosphere) the polar vortex plays some role in the transport of dust and sublimated CO_2 ice between the surface and atmosphere (D. M. Mitchell et al. 2015; S. D. Guzewich et al. 2016; A. D. Toigo et al. 2017; D. W. Waugh 2023), while in Titan's atmosphere the polar vortices play a role in the condensation of hydrocarbons from the mesosphere down into the stratosphere and potentially to the surface (N. A. Teanby et al. 2019; S. Vinatier et al. 2020; J. Shultis et al. 2022; D. W. Waugh 2023). The polar vortices on Venus, the remaining terrestrial planet with a substantial atmosphere, are substantially different from those on Earth, Mars, and Titan. The Venus polar vortices are much smaller, do not have a strong seasonality (consistent with small obliquity), and the morphology and centers of the vortices are highly variable (see D. M. Mitchel et al. 2021 and references within). The dynamics of these vortices is thought to be more similar to Earth's tropical cyclones than Earth's polar vortices.

The structure of a polar vortex is often described by its associated potential vorticity (PV), which is a useful dynamical field that is analogous to angular momentum within a fluid (air parcel), and can be used to diagnose the structure and evolution of the vortex. PV is defined as

$$PV = \rho^{-1}\zeta_a \cdot \nabla\theta \approx \rho^{-1}\zeta_{a,z}\frac{\partial\theta}{\partial z} \quad (1)$$

where ρ is the fluid density, ζ_a is the three-dimensional (3D) absolute vorticity vector, $\zeta_{a,z}$ is the vertical component of the absolute vorticity, which is the sum of the relative vorticity (ζ) and planetary vorticity (f), and $\nabla\theta$ is the 3D gradient of potential temperature, with $\frac{\partial\theta}{\partial z}$ being the vertical component. PV is a useful tool for studying polar vortices for multiple reasons: first, PV is materially conserved for adiabatic, frictionless flows; second, other dynamical fields can be determined through PV inversion; and finally, PV gradients provide the restoring force for Rossby waves (e.g., B. J. Hoskins et al. 1985). As an adiabatically conserved quantity, PV is only created or destroyed through diabatic heating (such as latent heating or radiation) or frictional forces. Characterizing polar vortices by their zonally averaged PV distributions shows that they typically fall into two main categories: monopolar and annular. In a monopolar polar vortex, common on Earth, the

vortex starts out due to the onset of polar night, where the obliquity of the planet creates a period of time that leaves the polar region with no direct sunlight and causes the temperatures to plummet within the middle atmosphere, driving the spin-up of zonal winds due to this strong temperature gradient, and increasing PV within the polar regions where it is maximized at the pole. This vortex structure is generally more stable, with eddies and waves forming and breaking mostly along the outside or equatorward edge of the vortex, where the "edge" of the vortex is defined as the region of highest latitudinal PV gradient (M. E. McIntyre & T. N. Palmer 1983). The polar vortex is then maintained for the duration of winter until the sunlight returns to the polar regions and the temperatures rise, decelerating the zonal winds until the vortex breaks up in the spring. Alternatively, in the polar atmospheres of Mars and Titan, their polar vortices develop an annular structure, where the highest PV is offset from the pole in a ring with a negative latitudinal PV gradient poleward of that maximum, leading to a local polar minimum of PV (R. K. Achterberg et al. 2011). The resulting "donut" of larger PV is a generally unstable system which, in the absence of a restoring force or destruction of PV within the polar regions, collapses back to a monopolar structure (W. J. M. Seviour et al. 2017). On Mars the sublimation of CO_2 in the polar regions and the subsequent release of latent heating acts to destroy PV locally at the poles throughout the winter (A. D. Toigo et al. 2017). In Titan's middle stratosphere, the global overturning circulation locally heats the poles due to adiabatic compression and destroys PV over the poles during the winter (J. Shultis et al. 2022). There is large uncertainty in the PV structure of Venus' polar vortices, with no consensus on whether it is annular or monopolar (see D. M. Mitchell et al. 2021, Section 3.1.1, for discussion).

A key feature of the polar vortices on Earth, Mars, and Titan is that they create a mixing barrier, a region where the high winds associated with the edge of the vortex act to reduce the cross-vortex (equatorward or poleward) movement of air, isolating air inside the polar vortex from the air outside the polar vortex. However, the impact that an annular polar vortex structure, like those found on Mars and Titan, has on the transport of material across the vortex has yet to be thoroughly investigated. Recent work from E. R. Ball et al. (2023) indicated the presence of a mixing barrier in an idealized Martian atmosphere utilizing an effective diffusivity approach, where previously it had been thought that since these annular polar vortices are a generally more unstable system, there might be a more free flow of material into and out of the polar regions than there would be in a monopolar vortex (D. W. Waugh et al. 2019). Here we intend to test this hypothesis by answering the following questions: How does mixing across the polar vortex edge change with varying vortex structure? And is there agreement between models of increasing complexity, so as to provide a more robust answer to our primary question?

To answer these questions, we use both a two-dimensional (2D) shallow-water model as well as a 3D general circulation model (GCM), planetWRF, in order to generate polar vortices of varying PV structures and investigate any changes in the horizontal transport associated with those simulated polar vortices. To quantify the associated transport, we use a mixture of contour advection (CA) calculations and idealized passive decay tracers in each model framework. The different models are described in Section 2, and then in Section 3, we analyze the CA and idealized tracer results from the shallow-water model. In Section 4, we analyze a similar set of results for the 3D planetWRF model. Finally, in Section 5, we summarize our conclusions.

2. Models and Methods

In order to investigate the changes in transport due to varying polar vortex structure, we quantify horizontal transport in two separate ways: CA calculations and simulations of idealized passive tracers. We apply both of these methods of quantifying horizontal transport to models of increasing complexity, a 2D shallow-water model and a 3D GCM planetWRF, which have both been previously used to investigate polar vortices (W. J. M. Seviour et al. 2017; D. W. Waugh et al. 2019; A. D. Toigo et al. 2020).

2.1. Contour Advection Calculations

We use CA calculations to examine the horizontal stirring of material in and around polar vortices. This method is described in detail in D. W. Waugh & R. A. Plumb (1994), and has been used in a large number of studies examining stirring in Earth's stratosphere (W. A. Norton 1994; L. M. Polvani et al. 1995; A. Dethof et al. 2000; D. W. Waugh & P. Rong 2002; R. K. Scott et al. 2003). The method involves utilizing an initial field of a materially conserved property along with a 2D wind field in order to advect one or more contours of the selected field throughout the domain. In this study we use contours of PV in a vortex-centered "equivalent latitude" space, where the equivalent latitude is given by the latitude band which has a similar enclosed area to that of the PV contour. The contours are treated as a set of individual points which are then advected by the wind fields. As the contours evolve, small-scale features begin to develop and the spacing between individual points can increase, possibly leading to a separation too large to properly represent the contour. To overcome this issue, more points are inserted in between the original points in order for the contour to maintain a sufficient resolution.

In a chaotically evolving flow, the length of the contours increases approximately exponentially with time, e.g., $l(t) \approx l(0)\exp(\alpha t)$, where l is the length of the contour and α is the contour lengthening exponent, with units of time^{-1}, referred to herein as the "stretching rate." Following previous studies, we use this lengthening of contours as a measure of the stretching characteristics of the flow (P. Chen 1994; D. W. Waugh & R. A. Plumb 1994; D. W. Waugh & P. Rong 2002), where the strength of stirring is quantified by the stretching rate, e.g., less stirring results in a small stretching rate and more stirring results in a larger stretching rate.

2.2. Idealized Tracer Calculations

We further use idealized tracers to study the transport across the polar vortices. The tracers were initialized either inside the vortex as a circle spanning from a high-latitude band to the pole, or outside the vortex in a ring spanning from the equator to a low-latitude band, in order to investigate any directional biases in the evolution of the tracers. For the shallow-water model, we use an idealized conserved tracer since the simulations are only done over a short timeframe, where the initial concentration is set to 1 within the source region and then allowed to evolve with the flow. In planetWRF, we

employ an idealized time-decaying tracer due to the multiyear functionality of the model, where the massless passive tracer has a fixed mixing ratio of 1 within a defined source region and then undergoes uniform loss with a defined e-folding decay time everywhere outside of the source region as $dC/dt = -C/\tau$, where C is the mixing ratio of the idealized tracer and τ is the decay time constant (constant in time and space). Tracers of this type have been used to study polar vortices both on Earth and throughout the solar system (W. A. Norton 1994; A. D. Toigo et al. 2020).

2.3. Shallow-water Model

We start our investigations using the 2D shallow-water model. We use the same model configuration as W. J. M. Seviour et al. (2017). Although the focus of W. J. M. Seviour et al. (2017) was Mars, the simulations performed were more general, and cover polar vortices of differing PV structures. The model uses integrations of the rotating single-layer shallow-water equations on a sphere (W. A. Norton 1994; P. Rong & D. W. Waugh 2004; Y. S. Liu & R. K. Scott 2015; R. K. Scott 2016). In vorticity-divergence form, these equations are as follows:

$$\frac{\partial \zeta}{\partial t} = -\nabla \cdot (\mathbf{u}\zeta_a), \tag{2}$$

$$\frac{\partial \delta}{\partial t} = -\frac{1}{2}\nabla^2|\mathbf{u}|^2 + \mathbf{k} \cdot \nabla \times (\mathbf{u}\zeta_a) - g\nabla^2(h + h_b), \tag{3}$$

$$\frac{\partial h}{\partial t} + \nabla \cdot (h\mathbf{u}) = -(h - h_e)/t_r, \tag{4}$$

where ζ is the relative vorticity, δ is the divergence, and h is the layer thickness. Here $\zeta_a = \zeta + f = \zeta + 2\Omega\sin\varphi$, where Ω is the planetary rotation rate, φ is the latitude, g is gravity, and $\mathbf{u}$ is the 2D horizontal velocity. The system is forced by topography, h_b, and relaxes toward an equilibrium height profile, h_e, with a relaxation timescale given by t_r. For the shallow-water system, PV is defined as $q = \zeta_a/h$, therefore manipulating the height or thickness of the layer is the most efficient way of manipulating PV in this system.

All simulations are forced by topography with a zonal wavenumber of 2 and maximum amplitude at the equator to be more directly comparable to the conditions imposed in the PlanetWRF model (Section 2.4), and use a triangular spectral truncation with maximum total wavenumber of 85 (T85). The model is initialized with an equilibrium zonal height distribution that generates a zonal-mean annular PV profile which has a local minimum of PV near the winter pole, surrounded by an annulus of higher PV, and then a drop-off from the vortex edge to the equator. The shallow-water model is driven to relax to this equilibrium shallow-water height profile via the relaxation rate, dh/dt, that is inversely proportional to a relaxation timescale, t_r (Equation (4)). A long relaxation timescale means the system returns only very slowly toward its equilibrium state, and a short relaxation timescale means the system is driven very quickly toward its equilibrium state. We vary the relaxation e-folding timescale, t_r, of the system toward an annulus to manipulate the stability of the annulus, as well as varying the relaxation profile in order to manipulate the depth of the polar PV minimum and/or the radius of the annulus. As shown in W. J. M. Seviour et al. (2017), this process allows us to generate polar vortices of varying structure, strength, and type (i.e., monopolar or annular).

We conduct investigations of transport using the shallow model by applying both CA and idealized tracer calculations, as discussed previously. CA calculations are done over 10 sols and are initiated after the model has run for about 100 sols to reach a steady state, with output four times per sol. Simulations of idealized conserved tracers are also done in this framework utilizing an initial distribution of concentration, $c = 1$ for $80° < \varphi < 90°$, $c = 0$ for $\varphi < 80°$, and are run with no decay, i.e., $dC/dt = 0$, since this framework is run over a short period of time and to isolate differences in the pathways of transport between vortex structures to strictly the movement of the tracer.

2.4. PlanetWRF

We next use the more complex 3D planetWRF GCM (M. I. Richardson et al. 2007). For this study, we have chosen to use Mars-like conditions (A. D. Toigo et al. 2012) because within this setup it is possible to generate polar vortices of differing PV structure. This model setup includes a microphysical parameterization scheme in which deposition and sublimation of the main atmospheric constituent (equivalent to CO_2 in these simulations), and the subsequent exchange of latent heat, occurs when temperatures in the atmosphere fall below or rise above the deposition point. This allows us to toggle on and off the effect of latent heating in the Mars-like atmosphere, and thus change the PV structure of the middle atmosphere without significantly changing the global circulation (A. D. Toigo et al. 2017; D. W. Waugh et al. 2019). In the simulations including latent heating, the winter polar PV distribution becomes annular within the polar vortex and then moves toward being monopolar at higher altitudes, while in the simulations with no latent heating the winter polar PV distribution is monopolar throughout the whole altitude range (see Figure 5). This ability to activate the latent heating or not gives us control over the generation of polar vortices of different structures in 3D, similar to that possible in the 2D shallow-water model. This model setup allows stable use of a transverse map projection numerical grid (rotated pole) that displaces the mathematical poles of the projection to two antipodal locations on the equator so as to preserve a more accurate representation of the geographic poles (and thus the dynamics of the polar atmosphere). These simulations were done at $2° \times 2°$ spatial resolution and with 52 vertical levels spanning from the surface to approximately 3×10^{-2} Pa (3×10^{-4} hPa).

As with the shallow-water model, CA and idealized tracer calculations are both carried out with the 3D model. CA calculations encompassing 10 sols each are completed for a 90 sol period from $L_S = 240°$ to $L_S = 288°$, where a sol is the length of time for one rotation of the planet, and L_S is the planetocentric solar longitude, a measure of time denoted by the planet's position in its orbit around the Sun, with $L_S = 0°$ defined as the northern spring equinox. This period of time surrounds the northern winter solstice ($L_S = 270°$) and includes both the most developed stage of the polar vortex and the time leading up to it. These calculations were done on isentropic surfaces ranging from 250 K up to 500 K (~200 to 5 Pa pressure levels or ~9–40 Km altitude), which includes the altitude ranges typically associated with the polar vortex. The wind fields used were at a 2 hr temporal resolution. The contours used were typically between 20 and 25 individual PV

contours spanning from an equivalent latitude around 45° north to 85° north, with a higher concentration of contours placed around the peak PV gradient.

For the idealized tracer calculations, we use two different source regions in order to isolate the directionality of transport across the polar vortex, the first being a polar source region from 80°N to 90°N between 20 and 3 Pa pressure levels (30–44 Km altitude), and the second being an equatorial source region from the equator to 30°N between the surface and 3 Pa (44 Km altitude). For each source region, we employ an idealized tracer with a 1200 sol (approximately 2 yr for this Mars-like atmosphere) decay time constant in order to highlight long-term (interannual or multiseasonal) trends, rather than short-term (diurnal or weather) fluctuations, similar to A. D. Toigo et al. (2020).

3. Shallow-water Model Results

As shown in W. J. M. Seviour et al. (2017), the structure and variability of the polar vortex in the shallow-water model depends on the length of the timescale that sets the rate at which the shallow-water height relaxes to its initial equilibrium zonal profile (Equation (4)). By modifying the value of that relaxation timescale, different regimes of vortex structures can be formed. With a short timescale, a relaxation timescale of 0.25 sols, the PV structure very quickly relaxes back to a stable annulus of PV with a maximum PV value located off of the pole surrounding a local minimum (Figures 1(a), (b)). At a longer relaxation timescale of 0.7 sols, the annulus of the PV is more unstable as the longer relaxation time allows the annulus to collapse to a monopole of PV before eventually returning back to an annulus (Figures 1(c), (d)). Lastly, by extending the relaxation time to infinity, equivalent to removing the forced relaxation back to an annulus, the annulus of the PV collapses to a strong monopolar vortex with the maximum of the PV located at the pole (Figures 1(e), (f)).

3.1. Contour Advection

CA calculations are done for each of these scenarios, which gives insight into how the horizontal mixing varies with relaxation rate and thus vortex structure. An overview of the dynamics used in this model for the CA calculations can be found in W. J. M. Seviour et al. (2017). Starting with the strong-relaxation case (continually annular structure), outside the polar vortex there are generally high stretching rates, implying a region of high mixing in the surf zone of the vortex (Figures 1(a), (b)), where the surf zone is defined as the region of low PV gradient on the equatorward side of the polar vortex where wave-breaking events occur (M. E. McIntyre & T. N. Palmer 1983). This region of high stretching is then followed by a wide mixing barrier denoted by a region of low stretching rates colocated with the highest meridional gradient of the PV, which defines the vortex edge. Interior to that mixing barrier (poleward), stretching rates increase as the PV gradient becomes more shallow and eventually negative, allowing for the buildup of eddies and instabilities throughout the vortex interior to stir and increase the horizontal mixing locally (Figures 1(a), (b)). These results are similar to a recent study that investigated polar transport in an idealized Martian atmosphere, which showed elevated mixing on the interior and exterior of the vortex, as well as a region of no mixing colocated with the maximum PV gradient (E. R. Ball et al. 2023).

In the weaker-relaxation case with a more unstable annulus structure, a mixing barrier still exists within the region of the highest PV gradient, but is less strong and well defined. On the inside of the mixing barrier, where the PV gradient becomes flat and only weakly annular, there is higher mixing throughout (Figures 1(c), (d)). Finally, in the monopolar case where there is no relaxation back to an annulus, there are only high stretching rates outside the polar vortex in the surf zone, and generally no stretching from the vortex edge inward (Figures 1(e), (f)). In each of the annular cases, on either side of the mixing barrier the direction of filamentation is equatorwards toward the region of highest wind shear, consistent with M. Nakamura & R. A. Plumb (1994).

To investigate the effect of annulus geometry on horizontal mixing, we next hold the relaxation rate fixed at 0.25 sols and manipulate the relaxation profiles. Starting from the stable annulus structure with a strong relaxation, the profiles are modified by increasing and decreasing the polar annulus PV minimum, and widening the annulus by physically shifting the location of the annulus PV maximum toward the equator by 5° latitude (Figure 2).

CA calculations are then done on each of these new annular polar vortex structures. Starting with the deepened PV minimum (dashed line case shown in Figure 2), there are generally high stretching rates both inside and outside the vortex, with the highest values occurring on the interior along the extremely negative PV gradient, and a very thin mixing barrier persisting at the edge of the vortex along the maximum positive PV gradient (Figures 3(a), (b)). On the other hand, by reducing the PV minimum at the pole (dotted line case shown in Figure 2), the annulus evolves closer to a monopolar-type structure, and there is large broadening of the mixing barrier and much lower stretching rates throughout the polar vortex, with the highest stretching rates occurring on the outside of the vortex in the surf zone (Figures 3(c), (d)). Finally, by widening the radius of the annulus by 5° latitude to a range of 55°–65° (dashed–dotted line case shown in Figure 2), more of the initial contours are within the polar vortex interior so there is an almost constant stretching rate poleward of the maximum PV gradient, with elevated values on the outside of the vortex, and a minimum stretching rate again colocated with the maximum PV gradient (Figures 3(e), (f)).

3.2. Idealized Tracers

Simulations including idealized conserved tracers are performed using the previously described polar vortex structures to also visualize the horizontal transport. Once the model reaches a steady state, the tracer is initialized from 80°N to the pole and then run for an additional 90 sols, utilizing the monopolar vortex, annular vortex with strong relaxation, and annular vortex with weak relaxation (as shown in Figure 1). For the monopolar vortex, there is very little dispersion or mixing of the tracer at all throughout the polar region by the end of the 90 sol period, and it is clearly isolated within the confines of the polar vortex as defined by the PV field (Figures 4(a), (d)). Comparing the two annular cases, there is a notable difference in the amount of mixing occurring in the interior of the vortices. In the strong-relaxation case with a stable PV annulus structure, there is a shallow gradient of tracer concentration within the polar vortex, and the appearance of filamentation

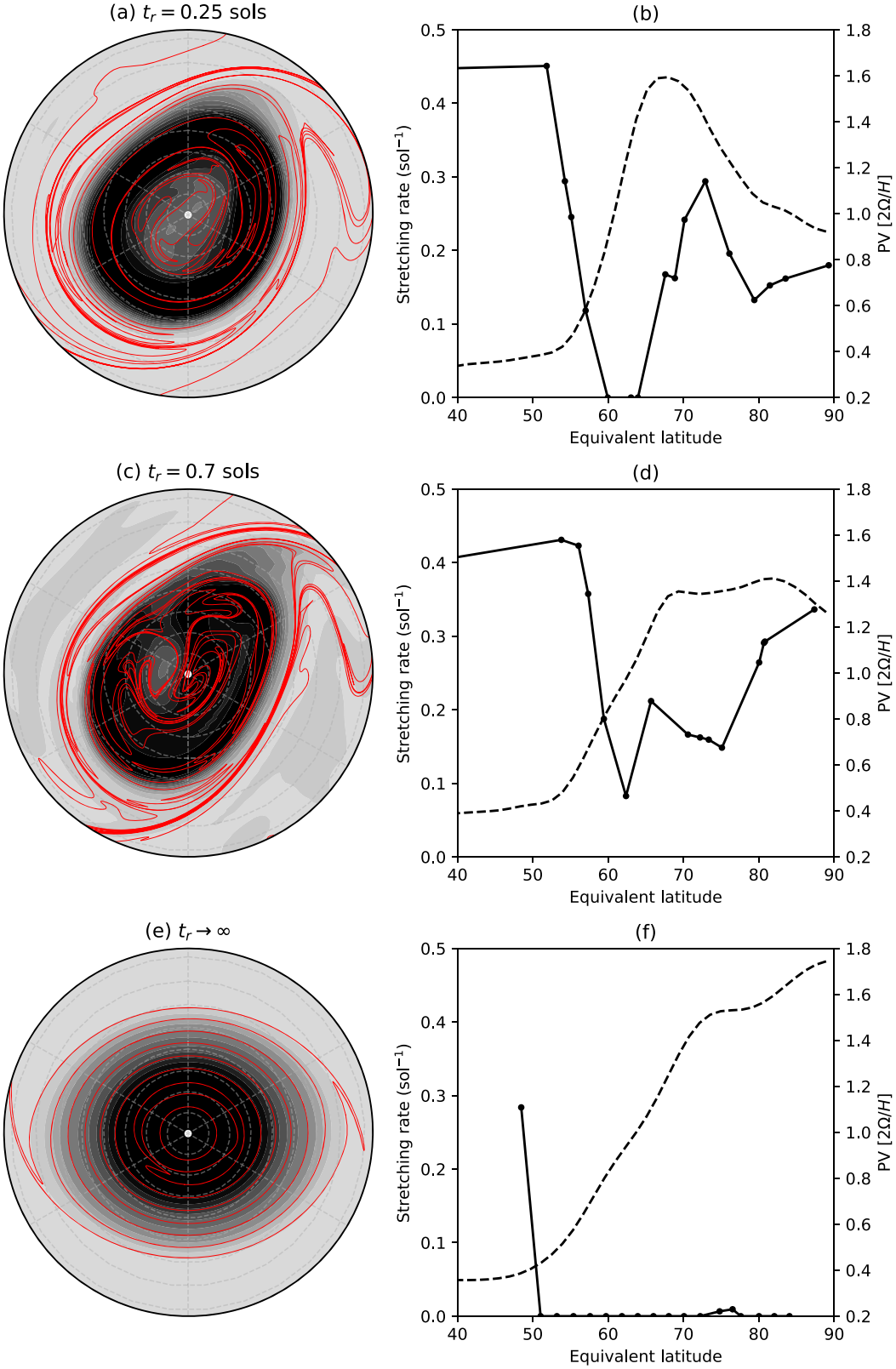

Figure 1. Shallow-water CA calculations of the three identified regimes. Left: initial PV contours after stretching for 4 sols (red contours) and instantaneous PV for the same time (grayscale shading); the stereographic map shows latitudes from 50° to the pole. Right: stretching rates (solid; left *y*-axis scale) and PV (dashed; right *y*-axis scale), for a stable annulus (a), (b), unstable annulus (c), (d), and monopolar vortex (e), (f). The PV values are scaled by the quantity $2\Omega/H$ (Ω is the rotation rate of the shallow-water model, and H is an imposed mean layer depth) to produce a unitless PV value that is comparable across different setups. Here a dip in stretching rates on the right is seen as a more circular contour on the left, denoting the location of the mixing barrier at the edge of the vortex.

along the region of negative PV gradient (decreasing PV with increasing latitude), which was not present in the monopolar scenario (Figures 4(b), (e)). However, in the case where there is weak relaxation and the PV structure moves back and forth between annular and monopolar, the tracer becomes very well mixed, with an even shallower gradient of tracer throughout the

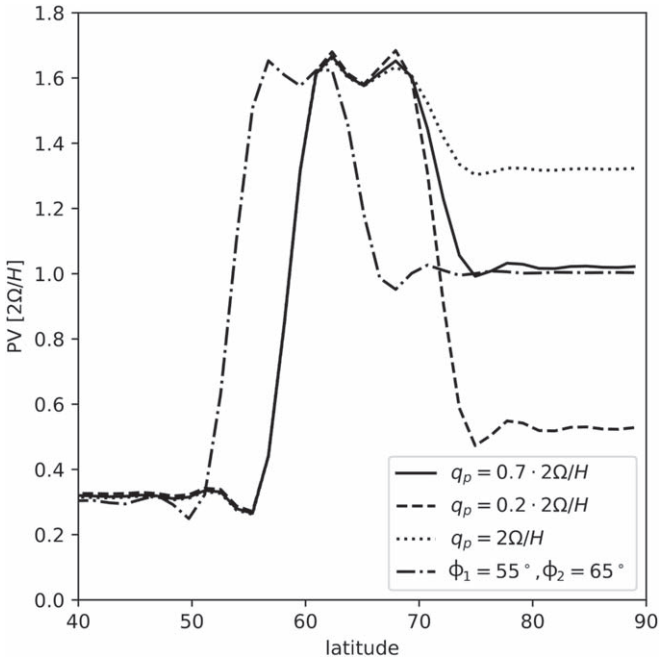

Figure 2. Modified annulus relaxation profiles used for Figure 3. Here q_p is the initial latitudinal PV profile function, and the plot shows the unmodified PV structure of the stable annulus from Figures 1(a) and (b) (solid), the deepened annulus (dashed), the weakened annulus (dotted), and the shifted annulus (dashed–dotted), with φ_1 and φ_2 being the new latitudinal edges of the shifted annulus. As in Figure 1, the quantity $2\Omega/H$ is a scaling factor to produce a unitless PV value that allows comparison of the PV across different setups.

polar vortex interior and a large amount of active filamentation (Figures 4(c), (f)). In these annular scenarios, the negative PV gradient does not act as a second mixing barrier, and instead there is increased instability and mixing within the polar vortex interiors. In all three of these polar vortex structures, the tracer remains isolated to the polar regions on the interior of the vortex edge. These tracer simulations agree with the previous CA results, indicating the presence of a mixing barrier in all three vortex structures.

4. PlanetWRF Model

Because the shallow-water model is limited to only a 2D representation of flow, we next explore the importance of 3D flow in the transport of material into and out of the polar vortex by using the planetWRF GCM to analyze similar measures of transport associated with polar vortices of different structures. As described previously, by turning the latent heating on or off in the model, we are able to change the PV structures of the polar vortex: With no latent heating there is a more Earth-like monopolar vortex where the PV is maximized at the poles, whereas with latent heating there is a more Mars- or Titan-like annular vortex where the PV maximum actually sits in a ring offset from the poles.

This is illustrated in Figure 5. Note, due to the dependence of PV on ρ^{-1}, the magnitude of PV increases rapidly with height, so we use Lait scaling (L. R. Lait 1994):

$$PV_S = PV\,(\theta/\theta_0)^{-(1+cp/R)}, \tag{5}$$

where θ_0 is an arbitrarily chosen potential temperature reference level, which we have chosen as $\theta_0 = 100$ K, and c_p/R is the ratio of specific heat at constant pressure to the universal gas constant, for which we use a value of $c_p/R = 4.0$, which is standard for the Martian atmosphere. At the 300 K isentropic surface (~70 Pa or 20 km) in these simulations, the annulus of the PV sits between 60–80°N, with a maximum PV value of around 3.5 PVU (Figure 5(a); 1 PVU $= 10^{-5}$ K m^2 kg^{-1} s^{-1}), while in the monopolar scenario the PV is almost double that amount, with a maximum value of around 6 PVU located at the north pole (Figure 5(b)). Both polar vortices have a ring of strong winds surrounding them, maximizing equatorward of the strongest PV gradients, with zonal wind speeds reaching about 100 m s^{-1} in the annular case and about 125 m s^{-1} in the monopolar case. The annular vortex remains annular from around the 500 K isentropic surface and below, but becomes monopolar above 500 K (Figure 5(c)), while the monopolar vortex is completely monopolar throughout the entire vertical range (Figure 5(d)). It should be noted that the isentropic surfaces curve strongly upwards in the polar regions (as denoted by a downward curve in the pressure contours), so horizontal motion along isentropes is really a mixture of horizontal and vertical motion in the physical atmosphere.

4.1. Contour Advection

Using output from these planetWRF simulations, we perform a series of 10 sol CA calculations covering a 90 sol period from $L_S = 240°$ to $L_S = 288°$ (late northern fall to early northern winter). Averaging over this entire window of time, both the annular and monopolar vortices show the presence of a mixing barrier (as denoted by a minimum in stretching rate) at the 300, 400, and 500 K isentropic surfaces (Figure 6). On average, there is a shift in the location of the mixing barrier between the two types of vortices by about 5° of equivalent latitude, with the annular polar vortex barrier being shifted equatorward of the monopolar vortex barrier.

We also see that there is slightly different behavior in the horizontal mixing depending on the isentropic surface chosen. Starting at the 300 K isentropic surface, where the annulus is clearly defined and remains a stable feature, the stretching rates in the annular polar vortex are much higher poleward of the mixing barrier inside of the vortex than they are on the equatorward side of the barrier in the free atmosphere or vortex surf zone (Figure 6(a)). In fact, on average the stretching rates are twice as high inside of the annular polar vortex than outside. At this same isentropic surface in the monopolar polar vortex, we see a different story where the highest stretching rates are on the equatorward side of the mixing barrier in the vortex surf zone, and there are generally lower stretching rates on the poleward side.

On the 400 K isentropic surface there is an increase in stretching rates within both polar vortices as wind speeds increase at this height, but both vortices maintain a region of highly reduced stretching indicative of a mixing barrier (Figure 6(b)). The stretching rates between the two polar vortices also become more similar in shape at this height, as the location of maximum stretching is now equatorward of the mixing barrier in both cases, but the annular polar vortex still maintains a region of higher stretching rates on the interior of the vortex. Finally, by the 500 K isentropic surface both polar vortices are monopolar in PV and share similar shapes of their stretching rate curves (Figure 6(c)). Here both polar vortices have high stretching rates within the vortex surf zone on the equatorward side of a very broad mixing barrier, and then

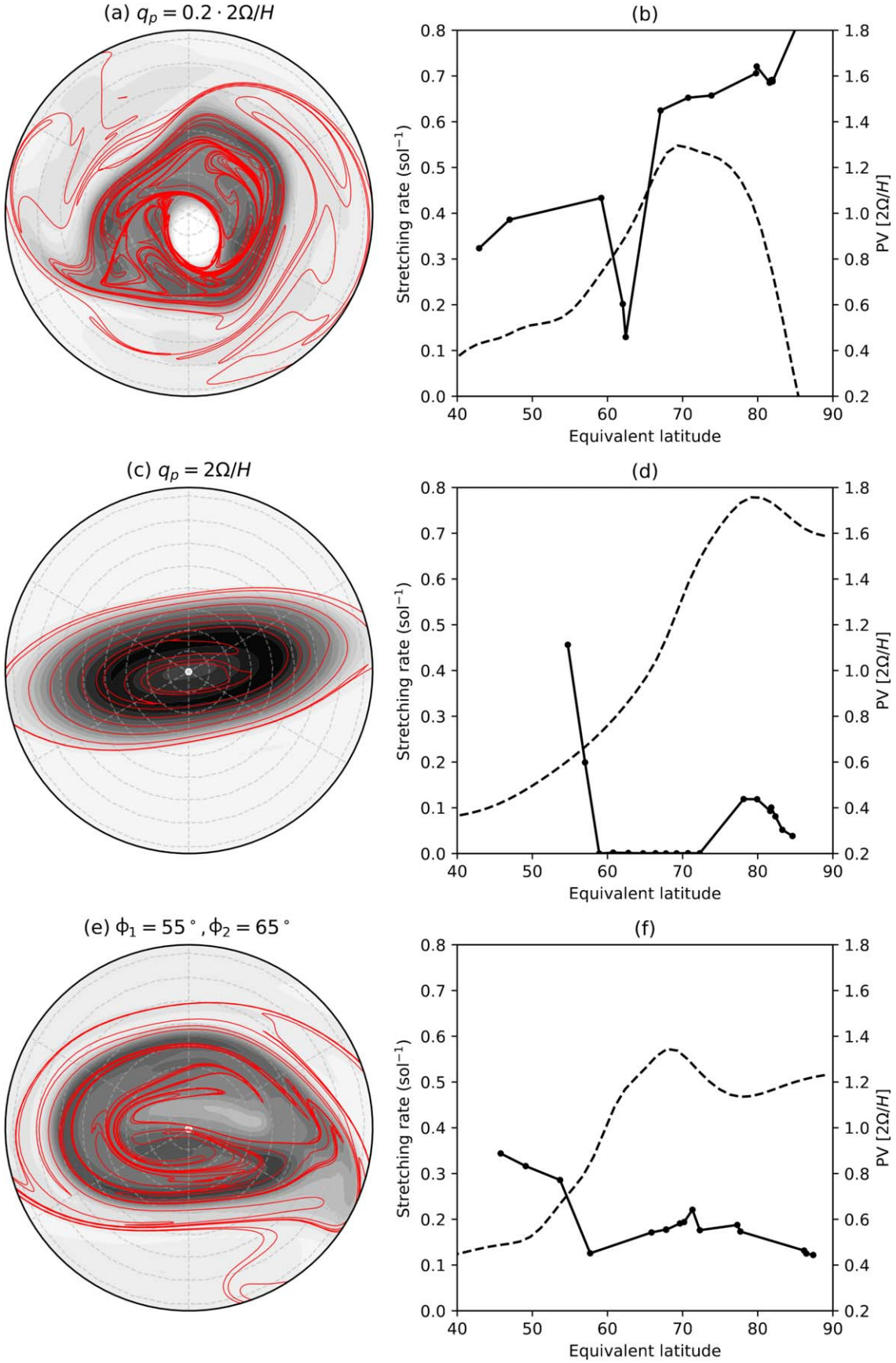

Figure 3. Similar to Figure 1, except for three perturbed relaxation profiles: deepened annulus (a), (b), shallow annulus (c), (d), and shifted annulus (e), (f).

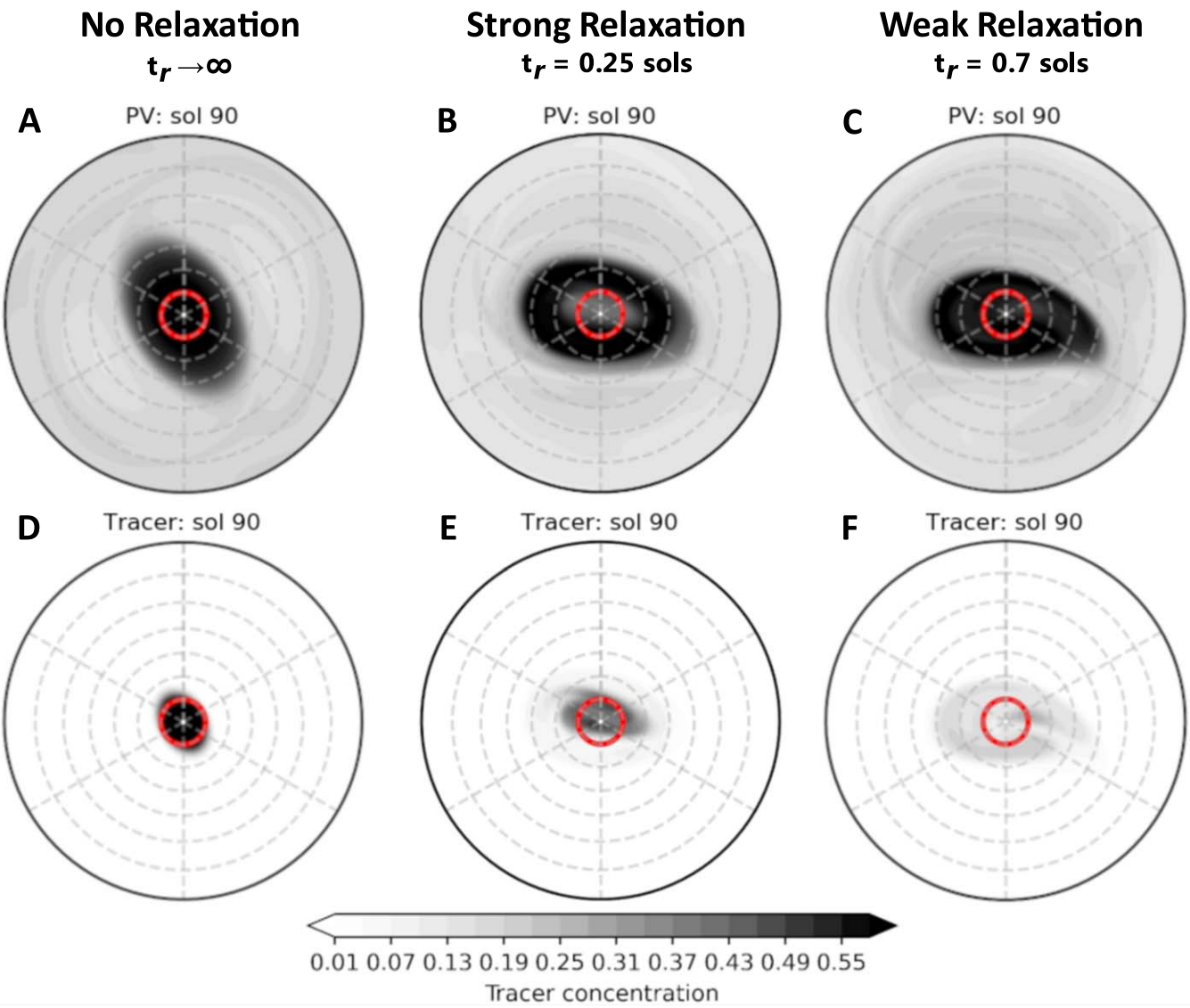

Figure 4. Shallow-water tracer simulations for the three previously identified scenarios after 90 sols, with initial tracer distribution north of 80° to the pole. Maps show a latitudinal range from 20° to the pole (90°). Note that in all cases the tracer is unable to escape the confines of the region of high PV, indicating the isolation of the polar region from the midlatitudes on the interior of the polar vortex edge.

elevated stretching on the far interior. The monopolar polar vortex appears to have higher stretching rates on average, most likely due to the slightly broader region of highest winds along the vortex edge. Once again, these results are consistent with E. R. Ball et al. (2023), which showed a similar behavior in an idealized representation of Mars' polar vortices.

We focus on the CA calculations initialized at $L_S = 267°$ and run until around $L_S = 272°$ (spanning the northern winter solstice when the polar vortex is at its strongest) to analyze the relationship between the stretching rates and the PV gradient in the different vortex structures. In general across all heights it is found that the minimum in stretching rates is colocated with the highest PV gradient (Figure 7), similar to the results from the shallow-water model. On the 300 K isentropic surface this peak latitudinal PV gradient occurs at roughly 62°N in the annular vortex and closer to 66°N in the monopolar vortex (Figure 7(c)), where in both cases there is the presence of a mixing barrier. This relationship is also visible by analyzing the progression of contours, where there is large filamentation outside both vortices followed by a region of no filamentation along the PV gradient, and then the annular polar vortex has large filamentation inside the vortex along the negative PV gradient while the monopolar polar vortex has very little filamentation approaching the pole (Figures 7(a), (b)). Moving upwards, it is seen that as the annulus in PV shrinks toward the pole, so too does the location of the mixing barrier in the annular polar vortex, as it follows the location of maximum latitudinal PV gradient. By the 400 K isentropic surface the annular mixing barrier has shifted poleward by about 3° as the peak PV gradient becomes more in line with the monopolar PV gradient (Figure 7(f)). At the 500 K isentropic surface, both polar vortices are monopolar and share very similar PV gradients and stretching rates across the vortices (Figure 7(i)).

Comparing these snapshots from planetWRF to the shallow-water model results (from Figure 1) shows that there is similarity between the models. The 300 K isentropic surface in the planetWRF annular scenario is similar to the strong-relaxation or stable annulus scenario from the shallow-water model, which showed a very similar evolution of stretching rates across the vortex. At first glance the 400 K isentropic

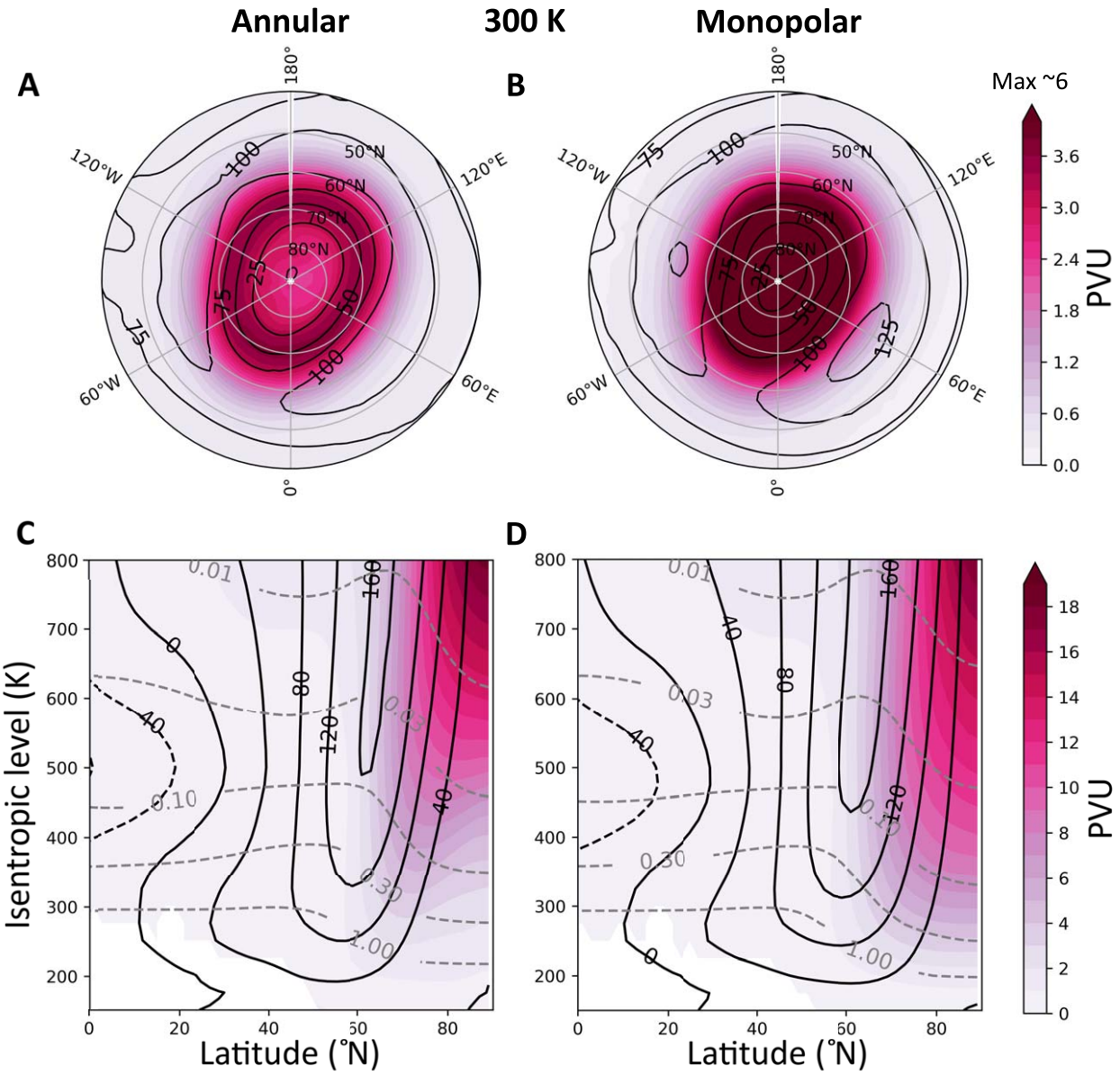

Figure 5. PlanetWRF scaled PV (1 PVU = 10^{-5} K m^2 kg^{-1} s^{-1}; fill) and zonal wind (in meters per second; black contours) averaged over 10 sols around the northern winter solstice ($L_S = 267° - 272°$) for simulations representing an annular vortex (a), (c) and a monopolar vortex (b), (d). Panels (a), (b): maps at the 300 K isentropic surface, extending from the pole to 40°N. Panels (c), (d): zonal averages; gray dashed contours are pressure surfaces in hectopascals.

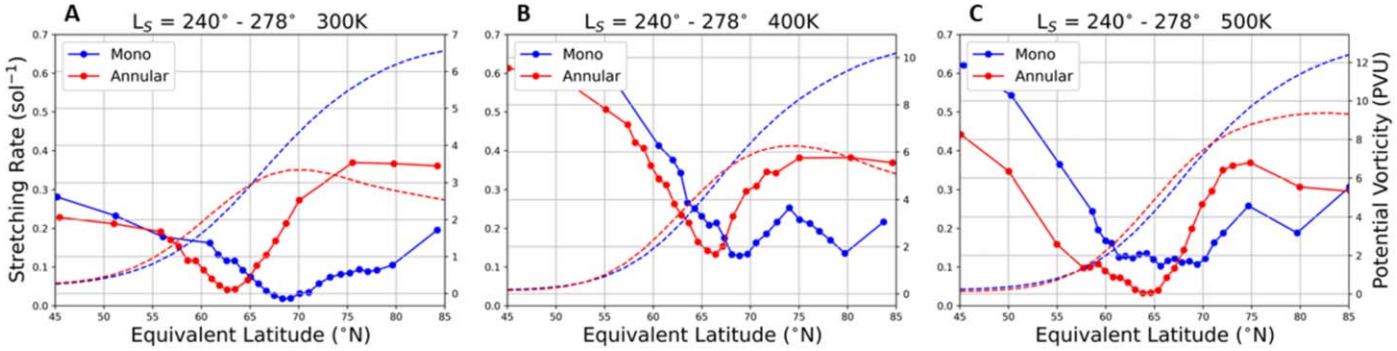

Figure 6. CA stretching rates (solid lines) and PV (dashed lines) averaged over the entire 90 sol calculation period for the 300, 400, and 500 K isentropic surfaces. Note that both vortices show a dip in stretching rates along the steepest latitudinal gradient of the PV. Also of note, the annular polar vortex becomes more monopolar with height, and the stretching rates become more similar between the two cases as well.

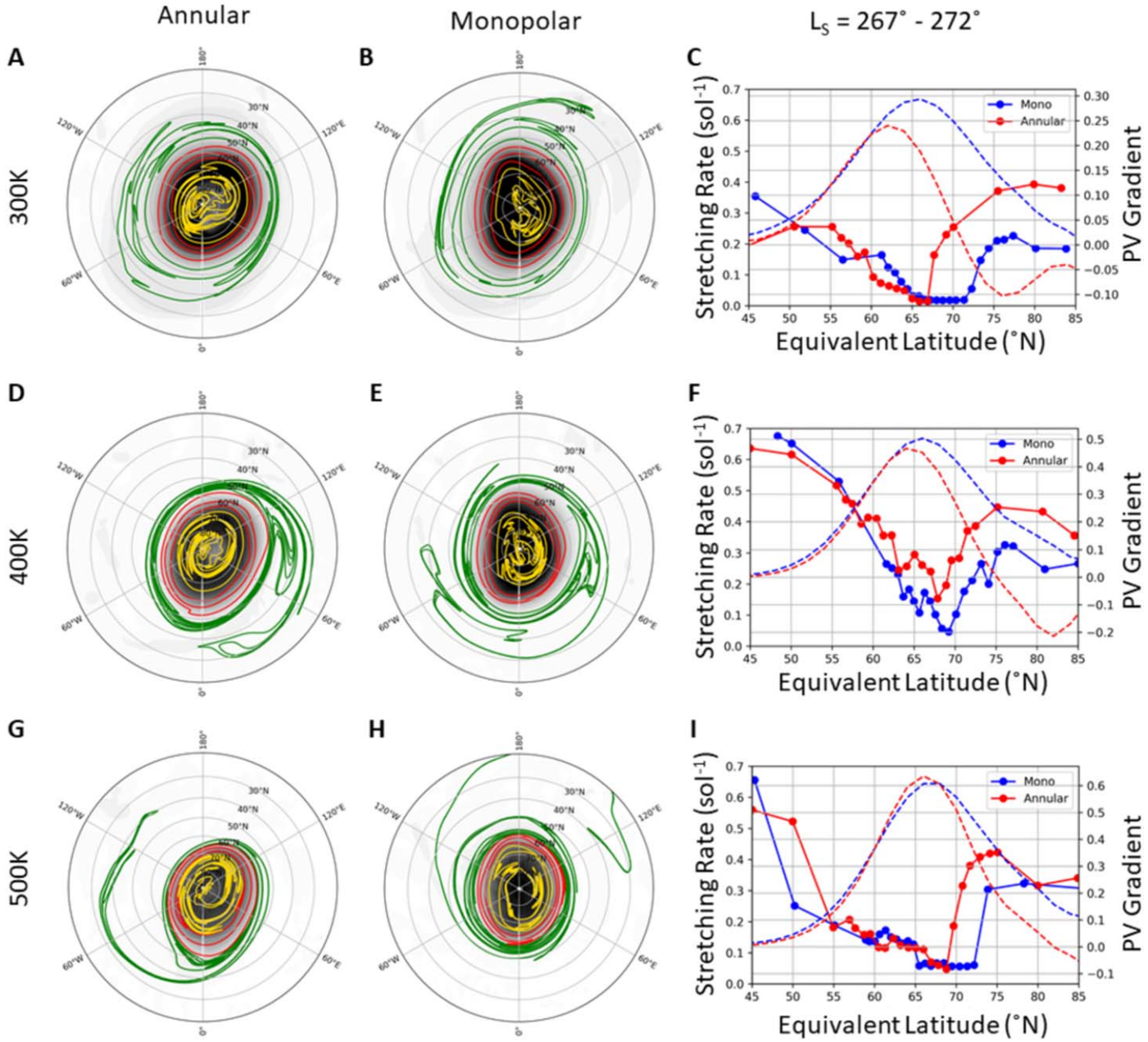

Figure 7. CA calculations for both the annular and monopolar scenarios at 300, 400, and 500 K isentropic surfaces initialized at $L_S = 267°$, with examples of contour progression after 3 sols for both annular (a), (d), (g) and monopolar (b), (e), (h) vortices with colors corresponding to similar regions of the vortices: outside vortex (green), vortex edge (red), and vortex interior (yellow). Stretching rates (per sol; solid line) vs. latitudinal PV gradient (10^{-5} K m^2 kg^{-1} s^{-1} deg^{-1}; dashed line) (c), (f), (i), with red lines notating the annular case and blue lines notating the monopolar case.

surface here shows similarities to the weak-relaxation scenario in the shallow-water model, at least in terms of stretching rates and PV, perhaps due to the fact that in planetWRF the annulus is becoming more monopolar with height so this level is at the cusp of that transition. However, the monopolar scenario in these planetWRF simulations is not as stable as in the shallow-water model, which only showed elevated stretching rates on the outside of the polar vortex, whereas there are always regions of higher stretching rates on both the equatorward and poleward sides of the monopolar vortex in the planetWRF model simulations. Also similar to the shallow-water model, filamentation on both the inner and outer edge of the annular polar vortex is equatorward, consistent with results showing that filamentation occurs in the direction of maximum wind shear (Figure 8). In both models this maximum wind shear is located equatorward of the vortex edge.

For this same time period ($L_S = 267°$ to $L_S = 272°$), CA calculations are done on additional isentropic surfaces to better investigate the vertical structure of the mixing barriers. These results reveal that the location of the mixing barrier in the annular polar vortex shifts poleward with height very strongly in the lower levels of the atmosphere where the polar vortex is in its stable annulus regime, before settling to a more constant latitude as the polar vortex becomes monopolar (Figure 9(a)). This shift in the location of the mixing barrier is consistent with the shift in the location of the maximum latitudinal PV gradient, which is pushed further equatorward where the annulus is strong and contracts toward the pole as the annulus

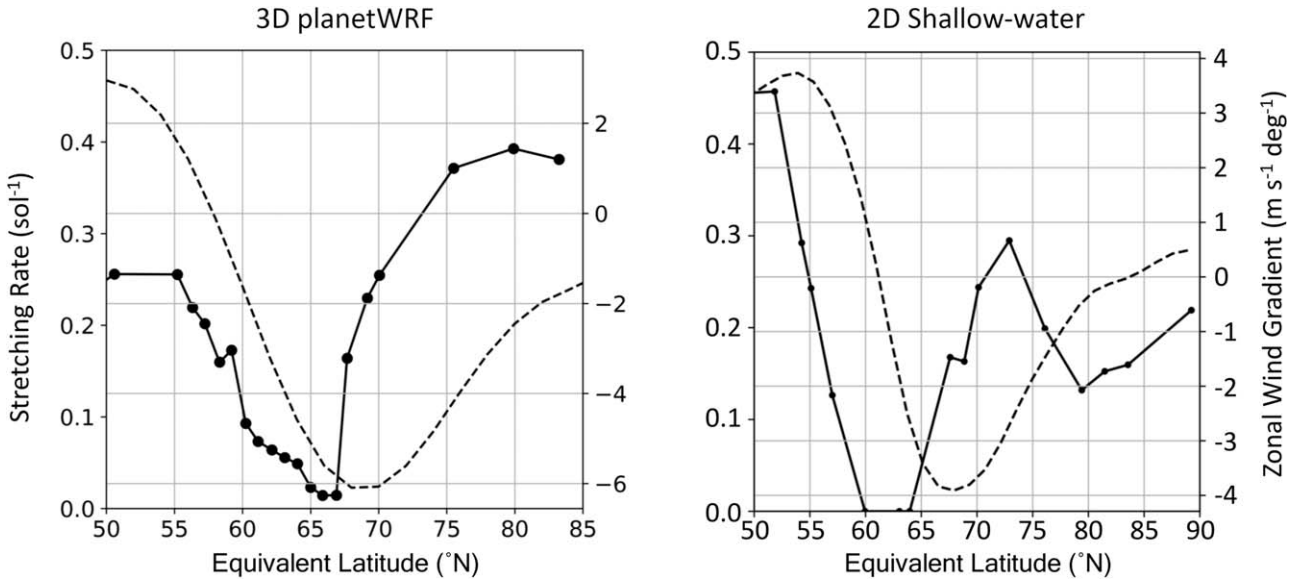

Figure 8. Latitudinal gradient of zonally averaged zonal wind (in meters per second per degree; dashed lines) and stretching rates (solid lines) for planetWRF at 300 K initialized at $L_S = 267^\circ$ (left) and shallow water with strong relaxation $t_r = 0.25$ (right) results. In both cases the maximum wind shear is equatorward of the mixing barrier at the polar vortex edge.

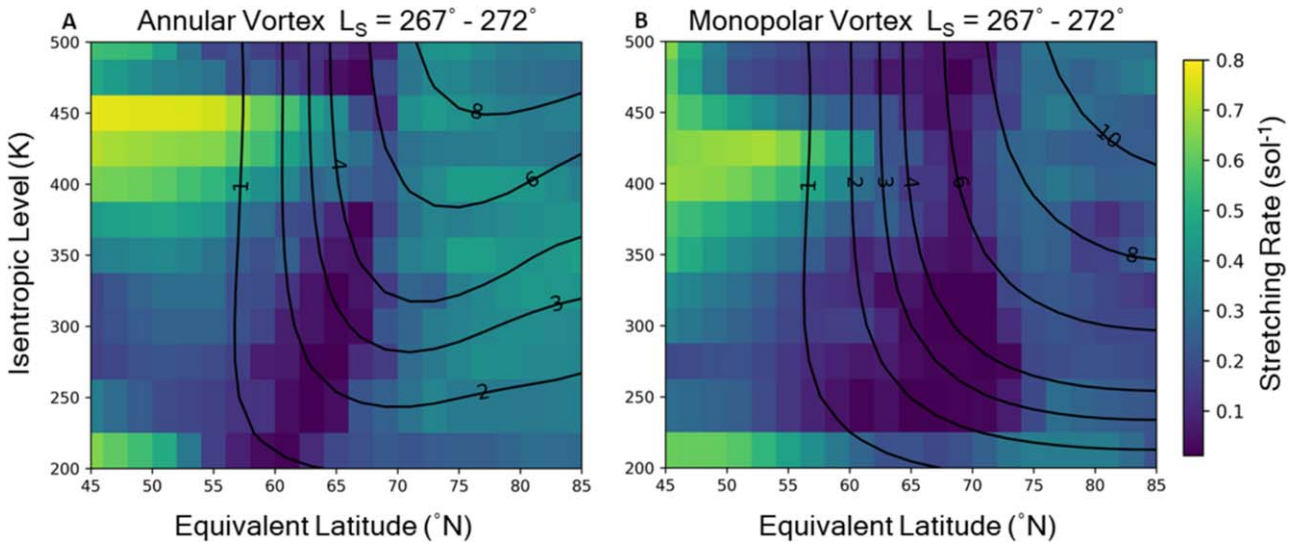

Figure 9. CA stretching rates (fill) and PV (contours) for the time period $L_S = 267^\circ$ to $L_S = 272^\circ$ for both the annular (a) and monopolar (b) vortices by isentropic surface and equivalent latitude. The annular polar vortex shows a sloping of the location of the mixing barrier toward the pole with height associated with the location of the maximum latitudinal PV gradient until it becomes more monopolar and the barrier is then more constant in space.

shrinks and eventually disappears, and is also consistent with results from E. R. Ball et al. (2023), which showed a similar shift in the location of the mixing barrier in an idealized modern Mars simulation. The monopolar polar vortex has a very vertically stacked mixing barrier, with no appearance of a shift or movement with height other than a narrowing at around the 400 K isentropic level. Once again this matches the location of the maximum PV gradient, which is much more constant in height in the monopolar polar vortex due to the higher values of PV.

There are two regions of elevated mixing noted during this time period, the lowest level analyzed at the 200 K isentropic surface (∼450 Pa or ∼2 km), and the 400–450 K isentropic levels (∼15–9 Pa or ∼31–37 Km). The 200 K isentropic surface is very low in the atmosphere and gets very close to intersecting the surface toward the equator, so this region of higher stretching is most likely caused by interactions with the surface flows, while the upper region has consistently higher stretching due to the increase in wind speeds and the poleward branch of the meridional overturning circulation.

Doing these CA calculations for multiple isentropic surfaces over a large period of time allows us to then analyze the temporal evolution of the horizontal mixing associated with these two different polar vortex structures. This analysis reveals that there are specific windows in time and height that the mixing barrier is reduced or moved in both polar vortices but never fully goes away, maintaining isolation of the polar air (Figure 10). On the 300 K isentropic surface, the time mean results hold pretty well for this entire period. The annular polar vortex shows a clear region of minimized stretching rates sitting along the region of maximum PV gradient around 60°–65° equivalent latitude, equatorward of the annulus, and the

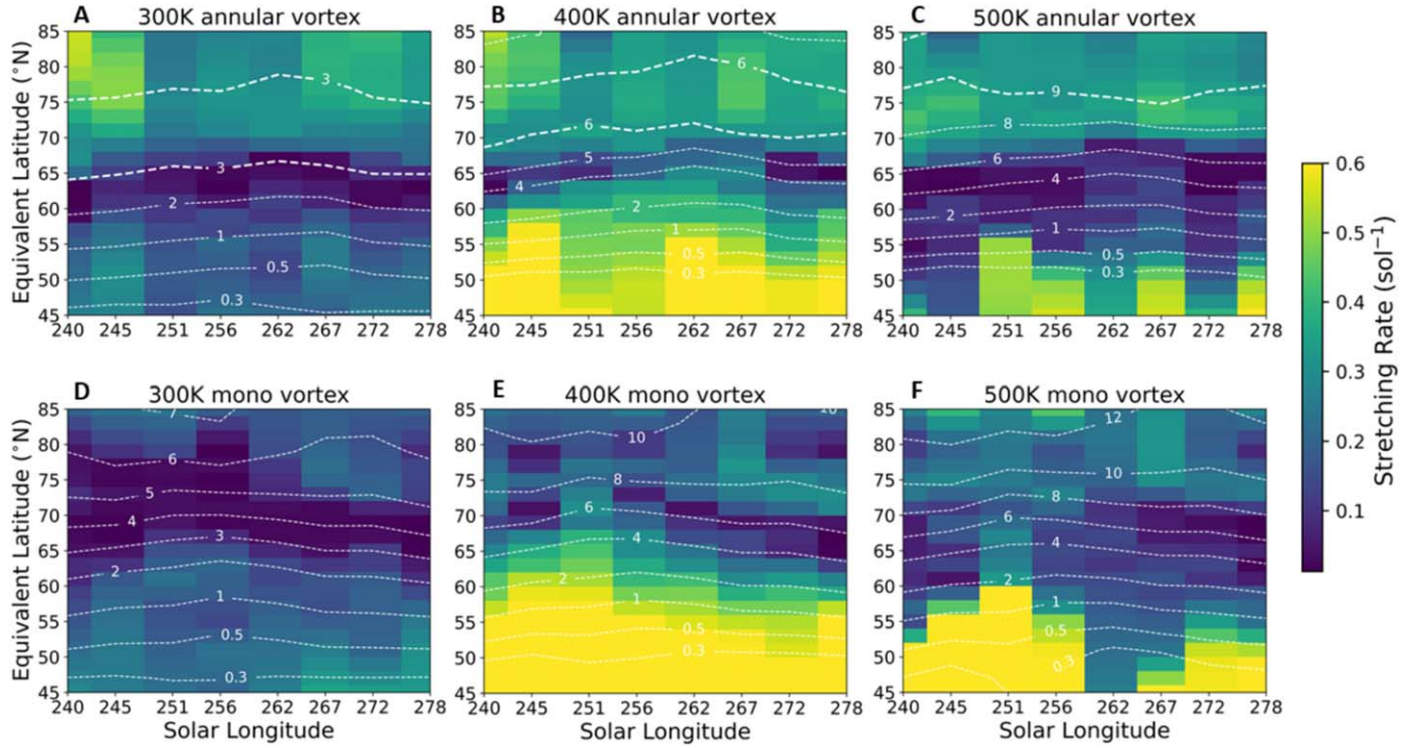

Figure 10. CA stretching rates (fill) and PV (contours) for both annular (panels (a), (b), and (c)) and monopolar (panels (d), (e), and (f)) vortices with time, for three isentropic surfaces of 300, 400, and 500 K. Over the course of this 90 sol period, both polar vortices maintain a mixing barrier associated with the strongest latitudinal gradient of the PV.

highest stretching rates on the interior of the annulus. The monopolar polar vortex has a broad mixing barrier associated with a very strong PV gradient (∼65°–78° equivalent latitude) for the first half of this time period (until $L_S = 262°$), and the mixing barrier can be seen to thin in the second half as there is a slight weakening of the PV gradient at higher equivalent latitudes. At the 400 K isentropic surface are the first signs of a weakening of the mixing barrier, with both polar vortices showing elevated stretching rates at different times. As was previously seen in the snapshots (Figures 7 and 9), very high stretching rates are seen outside of both vortices at this level for generally this entire window of time, however the monopolar vortex shows these elevated stretching rates making it further north early on when the PV gradient is strongest ($\sim L_S = 251°$), most likely due to a localized period of elevated wind speeds associated with the strong PV gradient, while the annular vortex shows elevated stretching rates as it gets closer to the winter solstice ($L_S = 256$–$267°$) where there is a poleward shift of the PV gradient. The interiors of both polar vortices remain isolated, however, as stretching rates within the polar regions remain fairly constant for this window of time, and there is a noticeable difference in stretching rates between the annular and monopolar polar vortices on the interior side of the mixing barriers. Finally, by the 500 K isentropic surface the annular polar vortex has become mostly monopolar in its PV structure, and the stretching rates between the two polar vortices are now fairly similar. The annular scenario still has slightly higher stretching rates on the poleward side of the mixing barrier, but the overall behavior between the two cases is very similar, with high stretching rates outside the vortex on the equatorward side of a broadened mixing barrier and lower stretching rates on the interior of the vortex, poleward of the barrier.

4.2. Tracer Transport

The CA calculations only provide a 2D method of investigating horizontal transport, and so we also include idealized decay tracers in our PlanetWRF model to measure horizontal transport and to further measure the difference between the two polar vortex setups. As was previously mentioned, we use two different tracer source regions in order to investigate any different pathways that the tracers may use to get into or out of the polar regions: an aloft polar source region and a column equatorial source region. The idealized tracers with a polar source have a source region from 80° north to the pole, and are placed vertically to be inside the strongest region of the polar vortex (20–3 Pa pressure levels or 30–44 Km altitude), in order to investigate how air that makes its way inside the vortices would disperse. All of these tracers are run for the same amount of time (90 sols) as the CA calculations, with an initialization at $L_S = 240°$.

By the end of this time period, by $L_S = 288°$, both the annular and monopolar polar vortices significantly isolate the tracers to the polar regions (Figure 11). In both vortices there is a sense of vertical motion and overturning inside the polar vortices in the tracer distributions, with the highest concentrations of tracer being just outside the source region south of 80° and then below the source region, with lower concentrations expanding in both vertical directions, hinting at weak upwards motion close to the pole and then stronger descending motion near the vortex edge. Looking at the annular polar vortex scenario, there is a clear slant toward the pole with the height of the highest tracer concentrations, indicating that the horizontal mixing occurring inside the vortex changes with height similar to what was seen in the CA results, with a shift in the location of the mixing barrier corresponding with the location of the

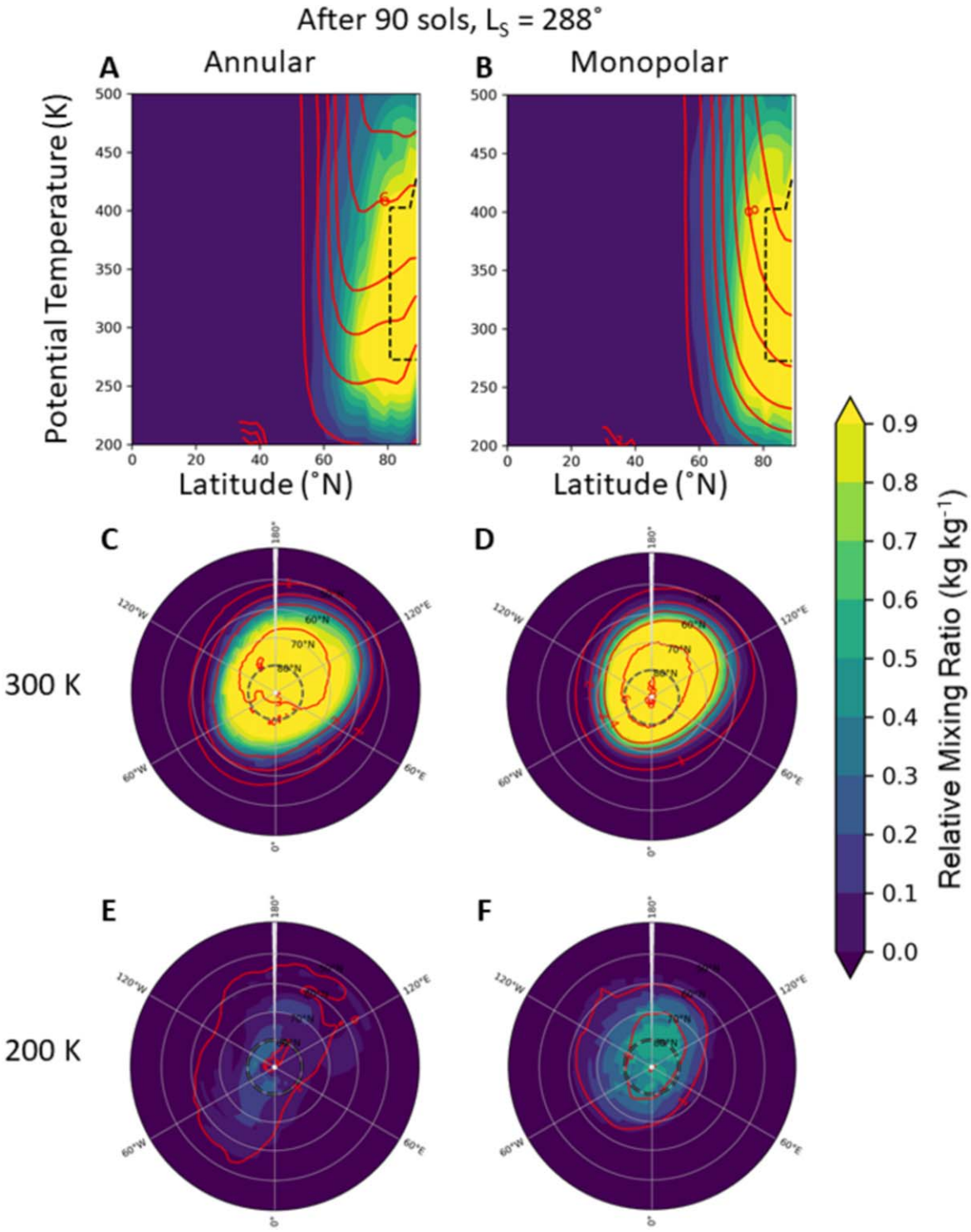

Figure 11. Idealized passive decay tracer with 1200 sol lifetime initialized from 80° north to the pole, showing the end of the 90 sol CA period. Panels (a), (b): tracer relative mixing ratio (fill) and PV (red contours) with height. Panels (c), (d): 300 K, and (e), (f): 200 K isentropic level distributions of tracer (fill) and PV (red contours). The black dashed line in all panels indicates the latitudinal limit of the tracer source region. By the end of this 90 sol period, the tracer remains isolated to the polar region with no sign of it crossing the polar vortex edge.

maximum latitudinal PV gradient. The monopolar scenario shows a much more vertically stacked distribution of tracer concentrations, which also mirrors the CA results. On the 300 K isentropic surface, the annular polar vortex shows a slightly weaker gradient of tracer concentrations and the presence of instabilities on the interior of the vortex edge, but no strong filamentation or excursions of tracer across the vortex edge. In the monopolar scenario, the tracer is much more evenly dispersed at this level and there is a strong gradient of concentrations right at the edge of the polar vortex. These polar source region tracer simulations agree with the shallow-water tracer simulations in the monopolar and strong-relaxation or

stable annulus cases after a similar amount of time. Nowhere in these polar source simulations is the tracer able to cross over the vortex edge and escape into the free atmosphere.

Tracer simulations with an equatorial source region are performed to investigate any potential transport pathways into the polar vortices from outside or below the polar vortex. In both polar vortices the primary direction for transport of tracer outside the vortex is poleward, until the tracer collides with the vortex edge and is forced to move vertically. By the end of the 90 sol period the tracer is able to fill up the region between the source region and the vortex edge, however the polar regions remain isolated aloft within the vortices (Figure 12). At the 300 K isentropic surface, both vortices show a similar gradient of tracer concentrations along the outside edge of the polar vortices, indicating the location of the mixing barrier.

However, there are elevated tracer concentrations on the inside of the annular polar vortex in the lower polar atmosphere that do not show up in the monopolar polar vortex. This feature has been observed previously in more Mars-focused studies (D. W. Waugh et al. 2019), where it was observed that there was a difference in the age of air tracer within the polar regions when comparing MarsWRF simulations with different parameterizations and resulting polar vortex structures. It was concluded that those differences were due to increased mixing across the polar vortex at that isentropic level. These equatorial source tracer simulations are instead indicating that there is movement of tracer from the free atmosphere down and under the polar vortex mixing barrier along the surface and lower atmosphere, and then ascending motion on the interior of the vortex is pulling the tracer upwards within the region of low PV inside the annulus. This difference is very clear when comparing the 300 and 200 K isentropic surface tracer distributions between both scenarios, where the annular polar vortex has a very large difference in the extent of the tracer distribution between 200 and 300 K but the monopolar polar vortex has only a slight difference between these two levels (Figures 12(c)–(f)).

This region just below the polar vortices (roughly below the 200 K isentropic surface in these simulations) can be defined as the subvortex, and appears to be where most poleward transport of tracer is occurring. There is similar behavior on Earth, where the monopolar polar vortex heavily isolates the south pole from the midlatitudes within the stratosphere, but it was found that there is a transition level where the subvortex region just below is actually capable of large amounts of mass transfer into and out of the polar regions (M. E. McIntyre 1995). This occurs on Earth around the upper troposphere/tropopause region of the atmosphere, where eddies drive the transport of air poleward. In our simulations a similar behavior is observed: There is strong isolation of the polar atmosphere aloft, but then almost free transport of tracer poleward between the surface and a transition level around the 200 K isentropic surface, where a small meridional overturning circulation cell on the interior of the vortex is generally forcing ascent (Figure 13). In the annular polar vortex scenario there is more transport of tracer into the polar regions than the monopolar scenario due to the fact that at these lower levels the monopolar polar vortex is stronger in terms of PV and as a result extends further downwards, limiting this subvortex transport to a shallower region. This difference is very clear by looking at the progression of tracer over time, where early on after the tracer was initialized ($\sim 6^\circ$ of L_S) there is more tracer within the polar regions under the annular vortex than the monopolar vortex (Figures 13(a), (b)), and again by $\sim 20^\circ$ of L_S since initialization the annular vortex maintains higher tracer concentrations below the polar vortex in the polar regions (Figures 13(c), (d)). Once the tracer is transported underneath the annular polar vortex, the enhanced mixing on the interior of the vortex associated with the negative PV gradient allows the tracer to be more easily transported upwards with the internal overturning circulation (Figure 13(e)), while in the monopolar polar vortex the vertical transport of the equatorially sourced tracer on the interior of the vortex is cut off much lower down (Figure 13(f)).

5. Conclusions

Polar vortices can exhibit two types of meridional PV profiles: monopolar vortices, where PV monotonically increases toward the pole, and annular vortices, where there is a local maximum of the PV that is offset from the pole. Annular vortices are created when the PV is destroyed locally within the polar regions, e.g., by latent heating from condensation of atmospheric gases (A. D. Toigo et al. 2017) or strong descent (J. Shultis et al. 2022). As discussed in Section 1, it has been hypothesized that an annular polar vortex has a reduced mixing barrier and more exchange of material between the polar regions and the extratropics than a monopolar polar vortex. Our analysis of both 2D shallow-water and 3D PlanetWRF simulations shows that annular and monopolar polar vortices both maintain a horizontal mixing barrier that isolates air within the polar vortex. Both annular and monopolar polar vortices show elevated mixing on the equatorward edge of the vortices, with a region of highly reduced or no mixing located along the steepest gradient of PV at the edge of the vortex. The region of positive PV gradient coincides with the region of fastest zonal winds, the jet core, the stability of which impedes cross-jet movement of air by pulling it into the jet direction. The main differences in mixing between the two polar vortex structures is in the interior of the vortices, where inside a monopolar polar vortex there was generally reduced mixing on the interior of the vortex edge, whereas inside an annular polar vortex there was a region of elevated mixing poleward of the vortex edge, and in some cases this region was actually where the highest levels of horizontal mixing occurred. This region of increased mixing develops where the PV gradient reduces in magnitude and becomes negative, as the zonal winds decelerate with latitude and eddies and instabilities are more easily generated. The PV gradient of a monopolar vortex also eventually reduces in magnitude; however, it never becomes negative, so large instabilities are not able to form. Thus, the sign and magnitude of the PV gradient is what appears to cause the mixing barrier, rather than just merely the magnitude, and no mixing barrier is observed in the region of negative PV gradient.

In the planetWRF simulations in the region below the polar vortices known as the subvortex, differences arose between the annular and monopolar polar vortices that indicate a potential pathway for material to enter the polar regions in this Mars-like atmosphere. Here we have hypothesized that air from the equatorial regions is able to move down (in the descending branch of the cross-equatorial Hadley cell) and poleward below the polar vortex, avoiding the mixing barrier region and then traveling along the surface where unstable eddies and topographical effects transport the air poleward, until it reaches a region of upwards motion on the interior of

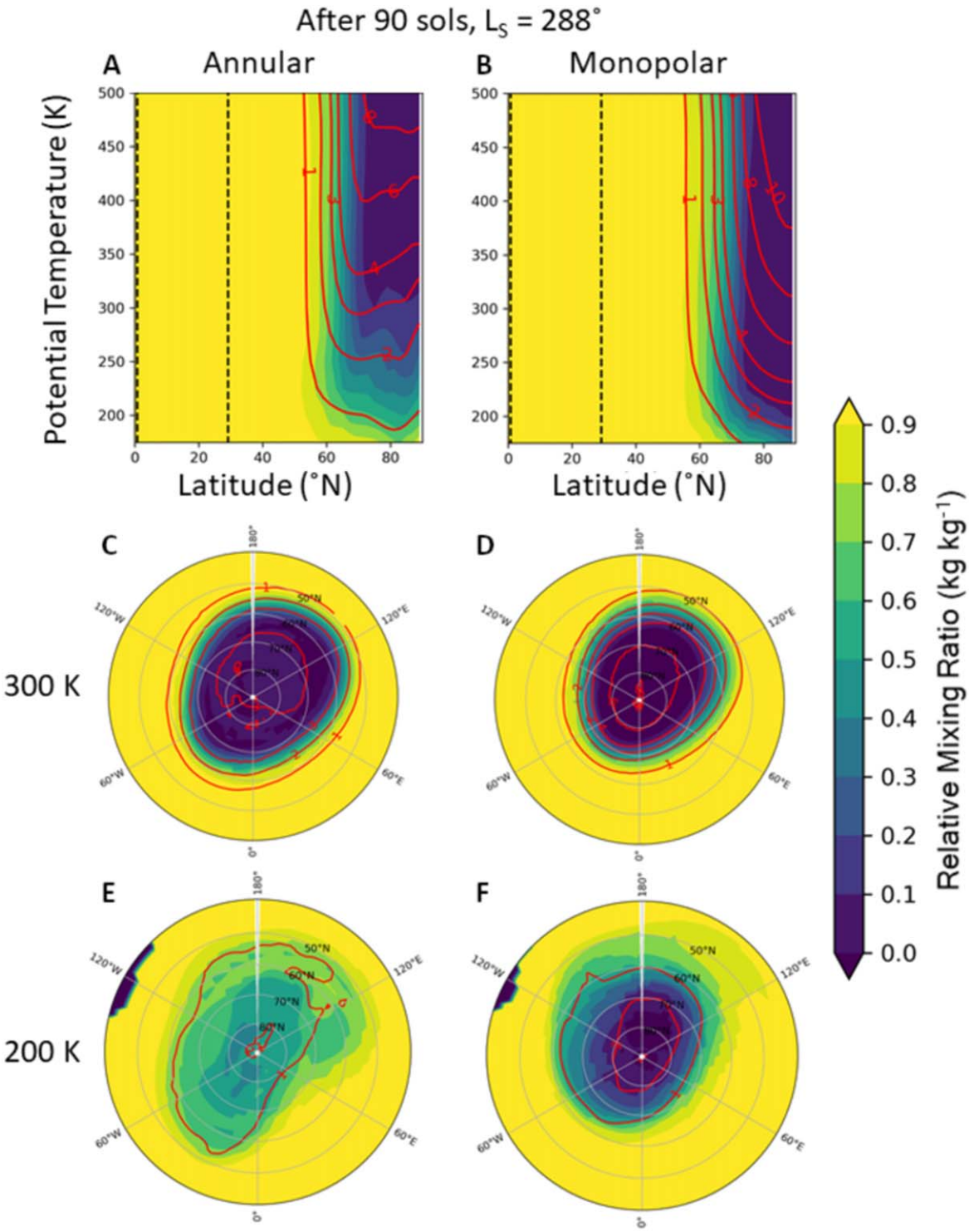

Figure 12. Idealized passive decay tracer with 1200 sol lifetime initialized from the equator to 30°N, showing the end of the 90 sol CA period. (a), (b): tracer relative mixing ratio (fill) and PV (red contours) with height. Panels (c), (d): 300 K and (e), (f) 200 K isentropic level distributions of tracer (fill) and PV (red contours). The black dashed line indicates the tracer source region. By the end of this 90 sol period, the polar regions aloft remain isolated from the midlatitudes, however below the annular polar vortex there is strong transport of tracers into the polar regions.

the vortex that transports that air upwards into the vortex. This pathway is much more viable in an annular polar vortex rather than a monopolar polar vortex due to the reduced vertical extent and the enhanced mixing of material on the interior of the annular polar vortex, while in the monopolar vortex the polar vortex extends further down and this upwards transport of material is cut off much lower in the atmosphere.

Although we start from a Mars-like atmosphere for simplicity and flexibility, our results found here should be applicable to many other terrestrial planets/moons. The presence of a mixing barrier regardless of the annularity of a

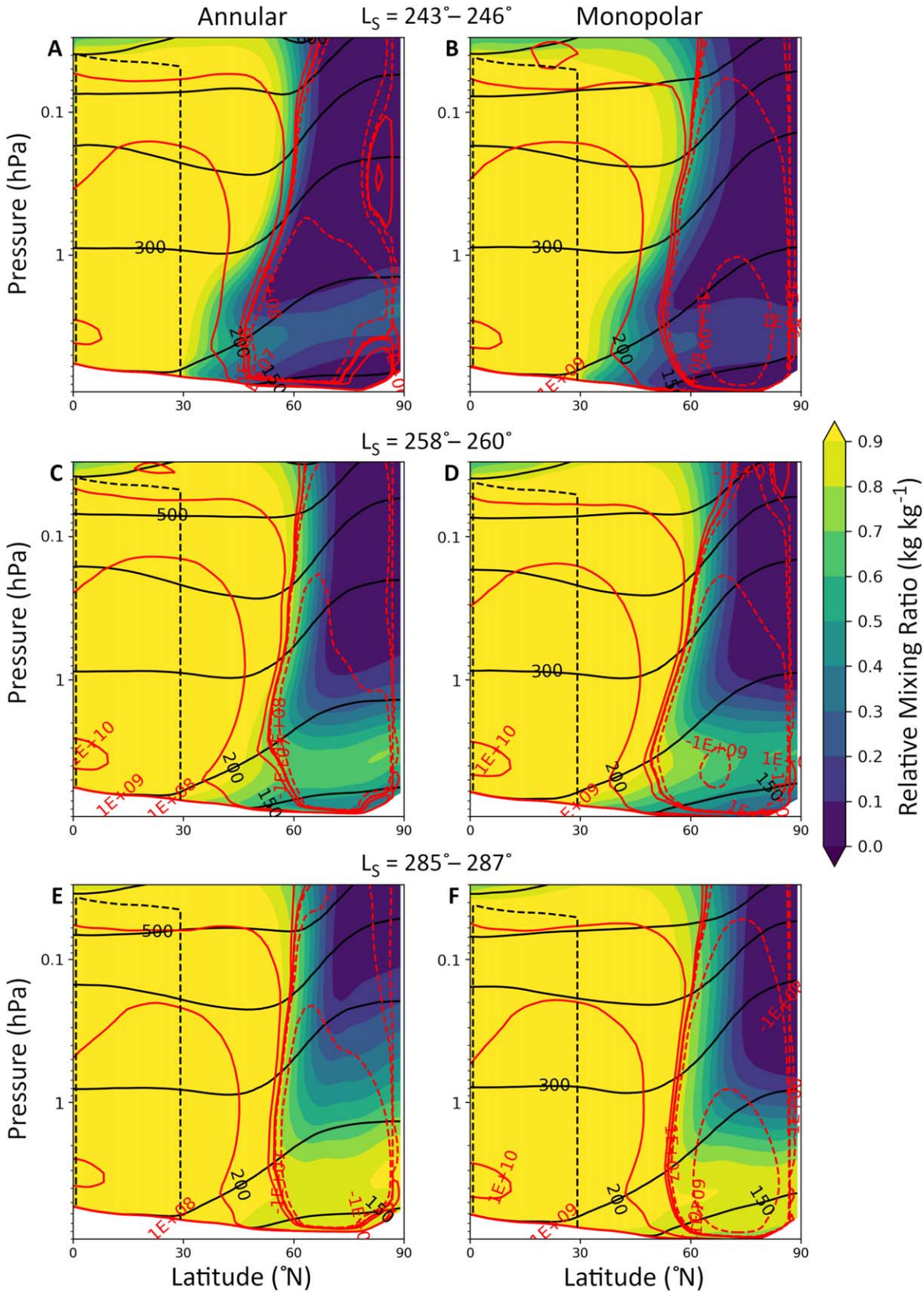

Figure 13. Idealized passive decay tracer with 1200 sol lifetime initialized at $L_S = 240°$ from the equator to 30°N now represented on pressure surfaces. Tracer relative mixing ratio (fill), meridional stream function (red contours; solid lines mean clockwise circulation and dashed lines represent counterclockwise circulation), and potential temperature surfaces (black contours) all averaged over 5 sol periods for three different time periods. The black dashed line indicates the tracer source region. In the subvortex region of both polar vortices there is transport of tracer from the midlatitudes into the polar regions, however in the annular case this tracer is then able to make its way upwards into the polar vortex interior.

polar vortex has implications for a variety of planetary bodies including Mars and Titan. In Mars' atmosphere, these results may assist in explaining the level of isolation within the polar vortex and highlight the importance of understanding the subvortex region when discussing the transport of material into and out of the vortex. Titan's atmosphere has a slightly different general circulation than the modeled atmosphere in this study, however its polar vortex also has periods where it becomes annular (J. Sharkey et al. 2021) and so may exhibit a similar movement of material in and around the vortex. In the future we plan to perform a similar set of experiments using Titan-specific models to investigate differences in the transport of material between the polar regions and the extratropics due to Titan's polar vortices throughout its seasonal cycle. Whether the results also carry over to polar vortices on other planets in our solar system (including Venus or the gas giants) or other solar systems is an open question.

Acknowledgments

The authors acknowledge NASA Solar System Workings grant Nos. 80NSSC20K0138 and 80NSSC23K0669, as well as the Johns Hopkins University Applied Physics Laboratory Graduate Fellowship FNACCX37 for funding support to accomplish this work.

ORCID iDs

Jacob Shultis https://orcid.org/0000-0002-8657-2872
William Seviour https://orcid.org/0000-0003-1622-0545
Darryn Waugh https://orcid.org/0000-0001-7692-2798

References

Achterberg, R. K., Gierasch, P. J., Conrath, B. J., Flasar, F. M., & Nixon, C. A. 2011, Temporal Variations of Titan's Middle-Atmospheric Temperatures from 2004 to 2009 Observed by Cassini/CIRS, Icar, 211, 686
Ball, E. R., Seviour, W. J. M., & Mitchell, D. M. 2023, The Importance of Isentropic Mixing in the Formation of the Martian Polar Layered Deposits, PSJ, 4, 213
Chen, P. 1994, The Permeability of the Antarctic Vortex Edge, JGRA, 99, 20563
Dethof, A., O'Neill, A., Slingo, J. M., & Berrisford, P. 2000, Quantification of Isentropic Water-vapour Transport into the Lower Stratosphere, QJRMS, 126, 1771
Guzewich, S. D., Toigo, A. D., & Waugh, D. W. 2016, The Effect of Dust on the Martian Polar Vortices, Icar, 278, 100
Hoskins, B. J., McIntyre, M. E., & Robertson, A. W. 1985, On the Use and Significance of Isentropic Potential Vorticity Maps, QJRMS, 111, 877
Lait, L. R. 1994, An Alternative Form for Potential Vorticity, JAtS, 51, 1754
Liu, Y. S., & Scott, R. K. 2015, The Onset of the Barotropic Sudden Warming in a Global Model, QJRMS, 141, 2944
McIntyre, M. E. 1995, The Stratospheric Polar Vortex and Sub-vortex: Fluid Dynamics and Midlatitude Ozone Loss, RSPTA, 352, 227
McIntyre, M. E. 1989, On the Antarctic Ozone Hole, JATP, 51, 29
McIntyre, M. E., & Palmer, T. N. 1983, Breaking Planetary Waves in the Stratosphere, Natur, 305, 593
Mitchell, D. M., Montabone, L., Thomson, S., & Read, P. L. 2015, Polar Vortices on Earth and Mars: A Comparative Study of the Climatology and Variability from Reanalyses, QJRMS, 141, 550
Mitchell, D. M., Scott, R. K., Seviour, W. J. M., et al. 2021, Polar Vortices in Planetary Atmospheres, RvGeo, 59, e2020RG000723
Nakamura, M., & Plumb, R. A. 1994, The Effects of Flow Asymmetry on the Direction of Rossby Wave Breaking, JAtS, 51, 2031
Norton, W. A. 1994, Breaking Rossby Waves in a Model Stratosphere Diagnosed by a Vortex-Following Coordinate System and a Technique for Advecting Material Contours, JAtS, 51, 654
Plumb, R. A., Heres, W., Neu, J. L., et al. 2003, Global Tracer Modeling during SOLVE: High-Latitude Descent and Mixing, JGRA, 108, 8309
Polvani, L. M., Waugh, D. W., & Alan Plumb, R. 1995, On the Subtropical Edge of the Stratospheric Surf Zone, JAtS, 52, 1288
Richardson, M. I., Toigo, A. D., & Newman, C. E. 2007, PlanetWRF: A General Purpose, Local to Global Numerical Model for Planetary Atmospheric and Climate Dynamics, JGR, 112, E09001
Rong, P., & Waugh, D. W. 2004, Vacillations in a Shallow-Water Model of the Stratosphere, JAtS, 61, 1174
Scott, R. K. 2016, A New Class of Vacillations of the Stratospheric Polar Vortex, QJRMS, 142, 1948
Scott, R. K., Shuckburgh, E. F., Cammas, J. -P., & Legras, B. 2003, Stretching Rates and Equivalent Length near the Tropopause, JGRA, 108, 4394
Seviour, W. J. M., Waugh, D. W., & Scott, R. K. 2017, The Stability of Mars's Annular Polar Vortex, JAtS, 74, 1533
Sharkey, J., Teanby, N. A., Sylvestre, M., et al. 2021, Potential Vorticity Structure of Titan's Polar Vortices from Cassini CIRS Observations, Icar, 354, 114030
Shultis, J., Waugh, D. W., Toigo, A. D., et al. 2022, Winter Weakening of Titan's Stratospheric Polar Vortices, PSJ, 3, 73
Teanby, N. A., Sylvestre, M., Sharkey, J., et al. 2019, Seasonal Evolution of Titan's Stratosphere During the Cassini Mission., GeoRL, 46, 3079
Toigo, A. D., Lee, C., Newman, C. E., & Richardson, M. I. 2012, The Impact of Resolution on the Dynamics of the Martian Global Atmosphere: Varying Resolution Studies with the MarsWRF GCM, Icar, 221, 276
Toigo, A. D., Waugh, D. W., & Guzewich, S. D. 2017, What Causes Mars' Annular Polar Vortices?, GeoRL, 44, 71
Toigo, A. D., Waugh, D. W., & Guzewich, S. D. 2020, Atmospheric Transport into Polar Regions on Mars in Different Orbital Epochs, Icar, 347, 113816
Vinatier, S., Mathé, C., Bézard, B., et al. 2020, Temperature and Chemical Species Distributions in the Middle Atmosphere Observed during Titan's Late Northern Spring to Early Summer, A&A, 641, A116
Waugh, D. W. 2023, Fluid Dynamics of Polar Vortices on Earth, Mars, and Titan, AnRFM, 55, 265
Waugh, D. W., & Plumb, R. A. 1994, Contour Advection with Surgery: A Technique for Investigating Finescale Structure in Tracer Transport, JAtS, 51, 530
Waugh, D. W., Polvani, L. M., Polvani, L. M., et al. 2010, Stratospheric Polar Vortices, The Stratosphere: Dynamics, Transport, and Chemistry, 190 (Washington, DC: AGU), 43
Waugh, D. W., & Rong, P. 2002, Interannual Variability in the Decay of Lower Stratospheric Arctic Vortices, JMeSJ, 80, 997
Waugh, D. W., Toigo, A. D., & Guzewich, S. D. 2019, Age of Martian Air: Time Scales for Martian Atmospheric Transport, Icar, 317, 148